Supplementary Material

O-bridged $NiSe_2$/CQDs Composite Synergistically Triggers Interfacial Electrons Transfer to Promote H_2O_2 Electrosynthesis

Qianqian XU[1], Haihong ZHONG[2,*], Chunli LI[1], Rong JIANG[1,*], Yongjun FENG[1,*], Luis Alberto Estudillo-Wong[3]

1 State Key Laboratory of Chemical Resource Engineering, College of Chemistry, Beijing University of Chemical Technology, No. 15 Beisanhuan East Road, Beijing 100029, China

2 School of Chemistry and Chemical Engineering, Collaborative Innovation Center of Ecological Civilization, Hainan University, No. 58 Renmin Road, Haikou 570228, China

3 Departamento de Biociencias e Ingeniería, CIIEMAD-IPN, Instituto Politécnico Nacional, Ciudad de México C.P. 07340, Mexico

Corresponding authors: Haihong ZHONG; Rong JIANG; Yongjun FENG

E-mails: hzhong@hainanu.edu.cn (ZHONG); hazeljr@buct.edu.cn (JIANG); yjfeng@mail.buct.edu.cn (FENG)

Text S1 Electrochemical measurements in RRDE electrode

Electrochemical performance measurements were conducted using an ALS-2325 electrochemical workstation (ALS Co., Ltd., Japan) in a conventional three-electrode configuration, with 0.1 M KOH aqueous solution as the electrolyte. The three-electrode system was completed with a graphite electrode as the counter electrode (CE), a Hg/HgO electrode as the reference electrode (RE), and a rotating ring-disk electrode (RRDE, geometric area = 0.1256 cm^2) was coated with catalyst ink as the working electrode (WE). The catalyst ink was prepared by dispersing 4 mg of the catalyst and 4 mg of black carbon in a mixed solution containing 20 μL of 5 wt.% Nafion, 750 μL of deionized water and 250 μL of isopropanol under ultrasound for 2 h. Subsequently, a certain amount of catalyst ink was dropped onto the RRDE electrode and air-dried at room temperature to achieve a mass loading of 100 μg cm^{-2}.

Prior to electrochemical measurements, the 0.1 M KOH electrolyte was purged with high-purity Ar or O_2 for 30 min, and O_2 flow was maintained above the electrolyte surface during measurements to keep saturation. Cyclic voltammetry (CV) curves were carried out to activate the catalyst at a scan rate of 50 mV s^{-1} in Ar or O_2-saturated electrolyte. Linear sweep voltammetry (LSV) was performed within the potential range of 0.1-1.0 V at the disk electrode at 1600 rpm with a scan rate of 5 mV s^{-1} in O_2-saturated electrolyte, and setting a potential of 1.5 V at the ring electrode.

The H_2O_2 selectivity and electron-transfer number (n) were calculated using equations (1) and (2) as follows, respectively:

$$H_2O_2\% = \frac{200 \times I_{ring}/N}{|I_{disk}| + I_{ring}/N} \quad (1)$$

$$n = \frac{4 \times |I_{disk}|}{|I_{disk}| + I_{ring}/N} \quad (2)$$

Where I_{disk} and I_{ring} are the disk electrode current and ring electrode current, respectively. The collection efficiency of the RRDE was determined to be 42.4 % (N = 0.424). All potentials in this work were quoted versus reversible hydrogen electrode (RHE) according to the equation: $E_{RHE} = E_{Hg/HgO} + 0.098\ V + 0.059\ pH$.

The electron transfer number (n) was calculated using the Koutecky–Levich (K–L) equation (3) and (4) based on the disk current density and the rotation speed of the working electrode:

$$\frac{1}{j} = \frac{1}{j_L} + \frac{1}{j_K} = \frac{1}{B\omega^{1/2}} + \frac{1}{j_K} \quad (3)$$

$$B = 0.62nFC_0(D_0)^{2/3}\nu^{-1/6} \quad (4)$$

Where j, j_L and j_K are the measured, diffusion-limiting, and kinetic-limiting current densities, respectively. ω is the angular velocity. F is the Faraday constant (F = 96485 C mol^{-1}). D_0 is the diffusion coefficient of O_2 in the 0.1 M KOH solution (1.9×10^{-5} cm^2 s^{-1}). C_0 is the bulk concentration of O_2 (1.2×10^{-3} mol L^{-1}) and ν is the kinematic viscosity of the electrolyte (0.01 cm^2 s^{-1}).

Text S2 Practical H_2O_2 production in flow cells

Electrochemical experiments of H_2O_2 production were conducted in a continuous flow electrolytic cell to mimic practical working conditions. The cell featured a three-compartment configuration with a gas diffusion electrode (GDE) as the cathode, an anion exchange membrane (AEM, N115), and a Pt sheet as the anode. 1 mg of $NiSe_2$-O-CQDs-10:1 catalyst, 1 mg of activated carbon black, 250 μL of ethanol, and 40 μL of 5 wt.% Nafion solution were added to a 1.5 mL centrifuge tube, which was subjected to ultrasonic treatment for 30 min. A commercial gas diffusion layer (GDL, Toray TGP-H-060), with a hydrophobic polytetrafluoroethylene (PTFE) coating to facilitate gas diffusion) was cut into 1 × 1 cm^2 pieces and pre-treated at 120 °C for 1 h to remove residual moisture. The well-dispersed catalyst ink was drop-cast onto the hydrophilic side of the GDL using a microsyringe. The GDL was then air-dried at room temperature for 2 h, followed by vacuum drying at 60 °C for 1 h to ensure complete solvent evaporation (avoids binder cracking and maintains GDL porosity). The catalyst mass loading on the GDL was calibrated to 160 μg cm^{-2}. The GDE (cathode, working electrode), AEM, and Pt anode were stacked in sequence, with PTFE gaskets placed between each component to seal the cell and prevent electrolyte leakage. 1 M KOH aqueous solution (60 mL for both cathode and anode chambers) was circulated through the respective chambers using a peristaltic pump at a constant flow rate of 12 mL min^{-1}. High-purity O_2 gas was fed to the backside of the GDE (hydrophobic side) at a flow rate of 20 mL min^{-1}, allowing O_2 to diffuse through the GDL pores into the 1 × 1 cm^2 catalytic region. All H_2O_2 yield experiments were conducted using a CHI 760E electrochemical workstation (Shanghai Chenhua Instrument Co., Ltd.) under chronoamperometry or chronopotentiometry conditions.

Text S3 Quantitative detection of H_2O_2 yield

The concentration of H_2O_2 was quantitatively determined via the cerium sulfate ($Ce(SO_4)_2$) titration method. The underlying principle of this assay is based on the redox reaction between Ce^{4+} and H_2O_2 under acidic conditions: the yellow cerium(IV) ions (Ce^{4+}) are reduced to colorless cerium(III) ions (Ce^{3+}) upon reaction with H_2O_2, as depicted in Equation 3. Since the concentration of Ce^{4+} exhibits a direct correlation with its absorbance at a wavelength of 319 nm, UV-Vis spectroscopy was employed to quantify the Ce^{4+} concentration. The absorbance of each $Ce(SO_4)_2$ standard solution with well-defined concentration at 319 nm was then measured individually, and a standard curve (with absorbance as the ordinate and Ce^{4+} concentration as the abscissa) was subsequently constructed to establish the quantitative relationship between absorbance and Ce^{4+} concentration.

$$2Ce^{4+}+H_2O_2 \rightarrow 2Ce^{3+}+2H^{+}+O_2 \quad (3)$$

Following electrolysis for a predetermined duration, the electrolyte was sampled and mixed with a Ce^{4+} standard solution of fixed concentration and volume. The absorbance of the resulting mixture was measured at a wavelength of 319 nm using UV-Vis spectroscopy. Leveraging the pre-established standard curve, the residual concentration of Ce^{4+} in the mixture was quantified. Subsequently, the concentration of H_2O_2 that participated in the redox reaction with Ce^{4+} was calculated using the residual Ce^{4+} concentration and the stoichiometric ratio of the Ce^{4+}- H_2O_2 reaction (Equation 3). This derived H_2O_2 concentration directly corresponds to the amount of generated H_2O_2.

Text S4 Degradation experiments of Rhodamine B and Methylene Blue

The electrocatalyst was subjected to electrolysis for 1 h under galvanostatic conditions using a self-assembled flow cell. After electrolysis, the resulting electrolyte was acidified to a pH of 2–3 with sulfuric acid. In separate preparations, 10 mL of 60 mg L^{-1} Rhodamine B (Rh B) and 10 mL of 60 mg L^{-1} Methylene Blue (MB) solutions were each combined with 1 mL of 1000 mg L^{-1} $FeSO_4$ solution. Subsequently, 5 mL of the acidified electrolyte was introduced into each dye–$FeSO_4$ mixture. The degradation process was monitored under continuous stirring, with photographic records and UV-Vis measurements taken at time intervals of 0, 1, 2, 3, 5, 10, 15, and 20 min.

Text S5 Computational details

All theoretical calculations were performed via density functional theory (DFT) using the projector augmented plane-wave (PAW) method as implemented in the Vienna ab initio Simulation Package (VASP) [1]. The exchange-correlation potential was described by the Perdew–Burke–Ernzerhof (PBE) generalized gradient approximation (GGA) [2], while long-range van der Waals (vdW) interactions were accounted for via the DFT-D3 scheme [3]. A plane-wave cut-off energy of 400 eV was used, and the Kohn–Sham equations were solved iteratively with an energy convergence criterion of 10^{-6} eV. A 15 Å vacuum layer was added perpendicular to the sheet plane to avoid artificial periodic image interactions, and Brillouin zone (BZ) integration was conducted using a Γ-centered 2 × 2 × 1 k-mesh. All structures were fully relaxed until the residual force on each atom was < 0.03 eV/Å. Crystal Orbital Hamilton Population (COHP) analysis was performed with the Lobster code [4].

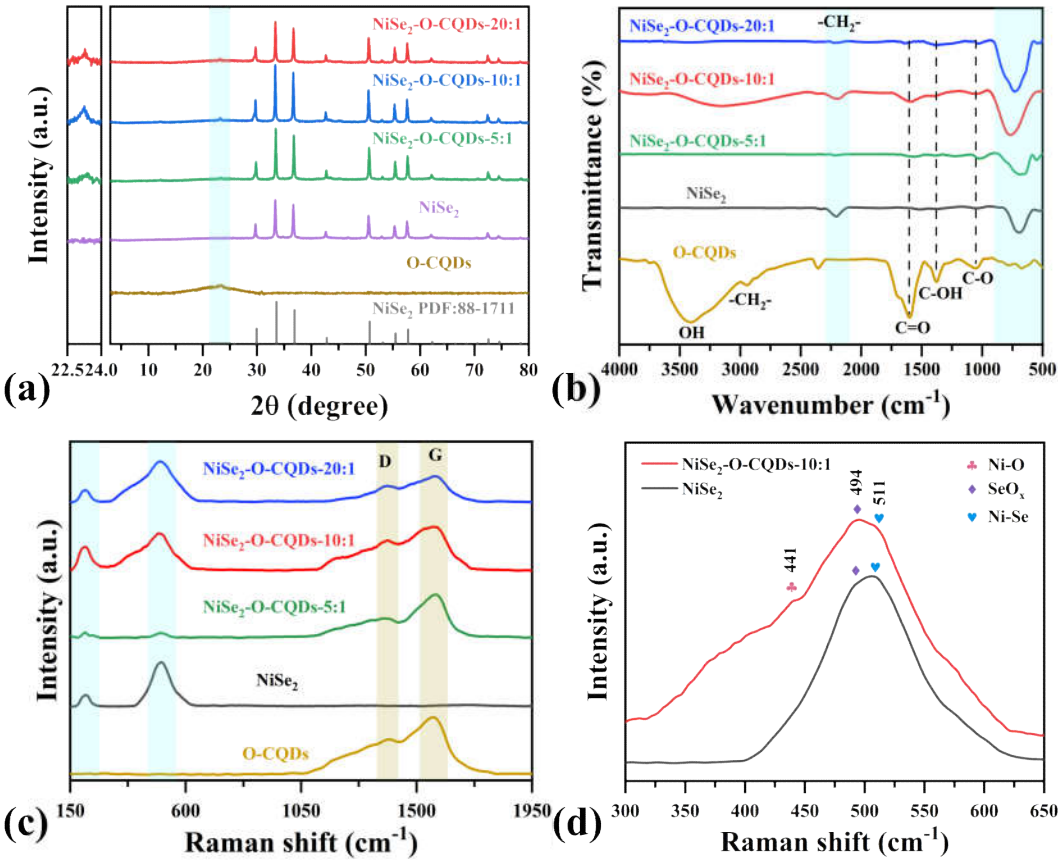

Fig. S1. (a) XRD patterns of $NiSe_2$, O-CQDs and $NiSe_2$-O-CQDs-*X*:1 (*X* = 5, 10, 20) samples. (b) FT-IR spectra. (c) Raman spectra. (d) Zoomed portion of Raman spectra on the $NiSe_2$ and $NiSe_2$-O-CQDs-10:1.

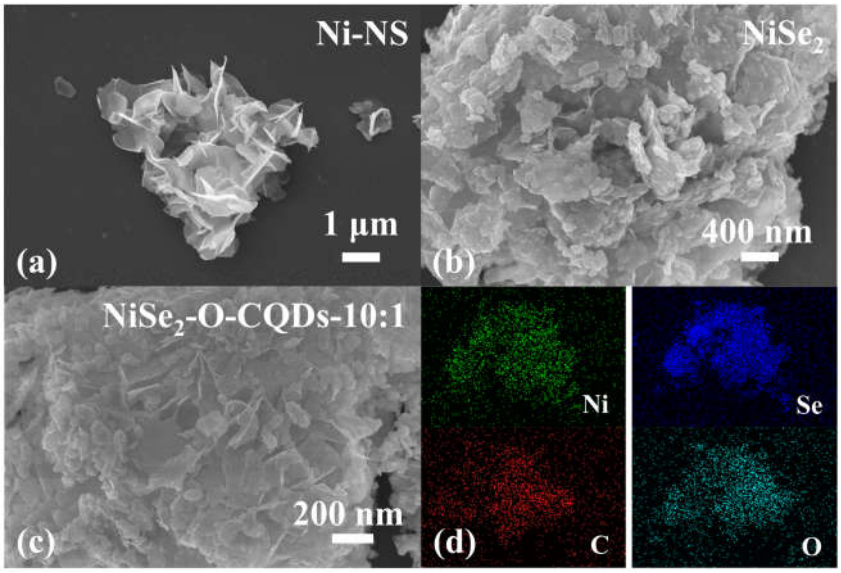

Fig. S2. SEM images of (a) Ni-NS, (b) $NiSe_2$ and (c) $NiSe_2$-O-CQDs-10:1. (d) EDX mapping of the $NiSe_2$-O-CQDs-10:1.

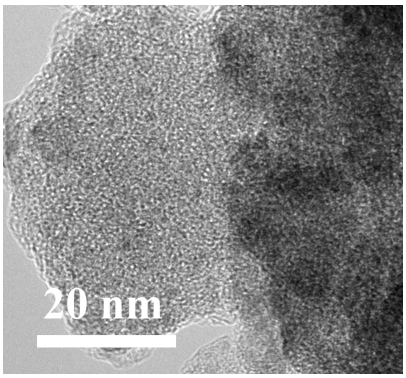

Fig. S3. TEM image of $NiSe_2$-O-CQDs-10:1 sample.

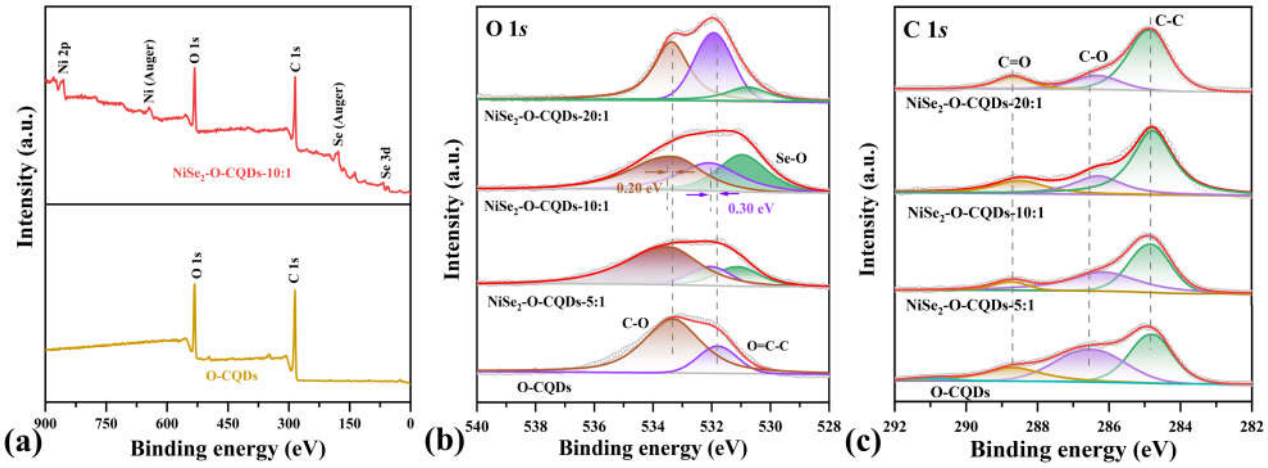

Fig. S4. (a) XPS survey of O-CQDs and $NiSe_2$-O-CQDs-10:1 samples. XPS spectra of (b) O 1*s* and (c) C 1*s* for $NiSe_2$, O-CQDs and $NiSe_2$-O-CQDs-*X*:1 (*X* = 5, 10 and 20).

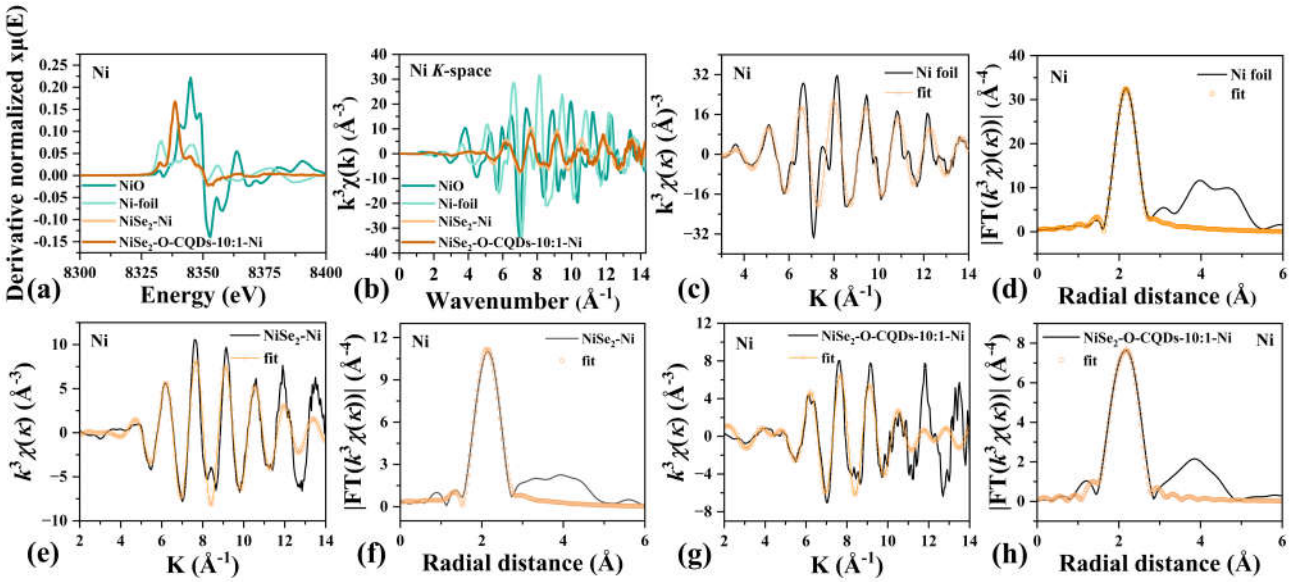

Fig. S5. *R*-space EXAFS fitting curves of $NiSe_2$ and $NiSe_2$-O-CQDs-10:1 at Ni *K*-edge.

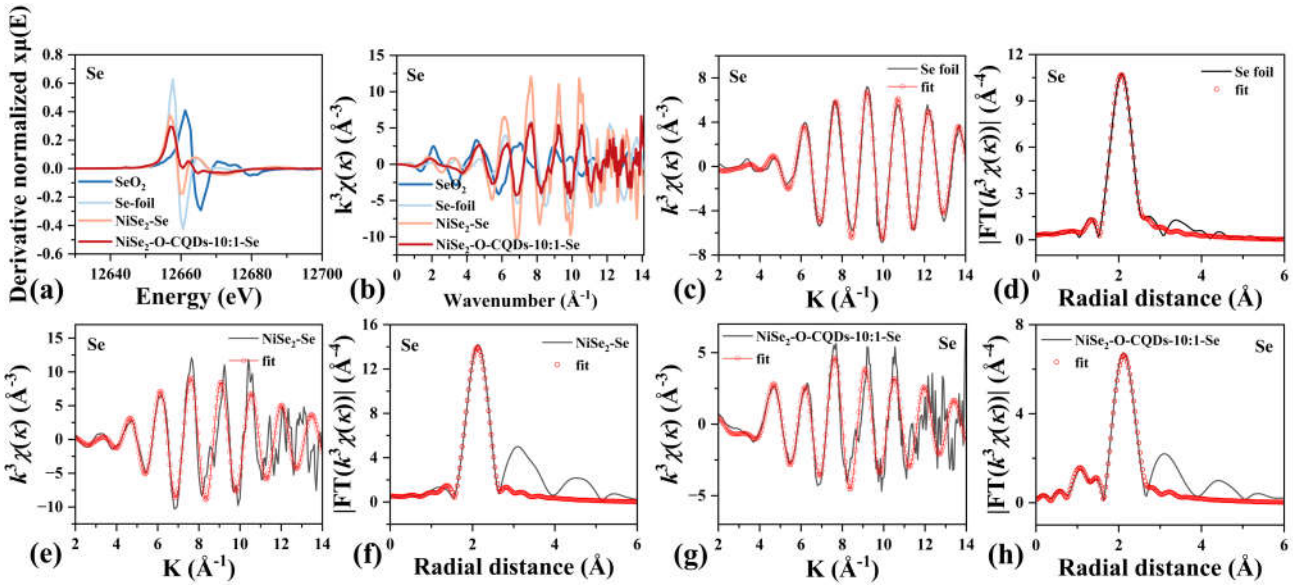

Fig. S6. *R*-space EXAFS fitting curves of $NiSe_2$ and $NiSe_2$-O-CQDs-10:1 at Se *K*-edge.

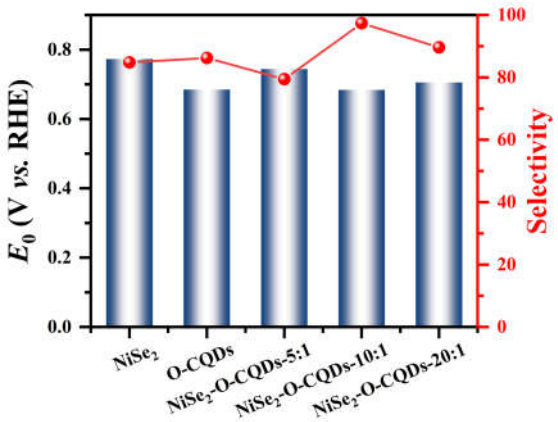

Fig. S7. Comparison of onset potential and calculated H_2O_2 selectivity (%) of $NiSe_2$, O-CQDs, and $NiSe_2$-O-CQDs-*X*:1 (*X* = 5, 10, 20) catalysts.

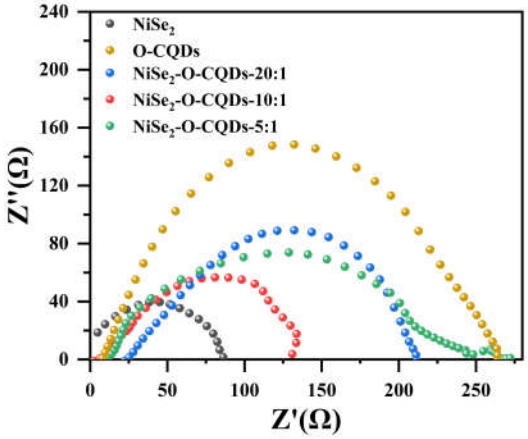

Fig. S8. EIS Nyquist plots of $NiSe_2$, O-CQDs, and $NiSe_2$-O-CQDs-*X*:1 (*X* = 5, 10, 20) catalysts.

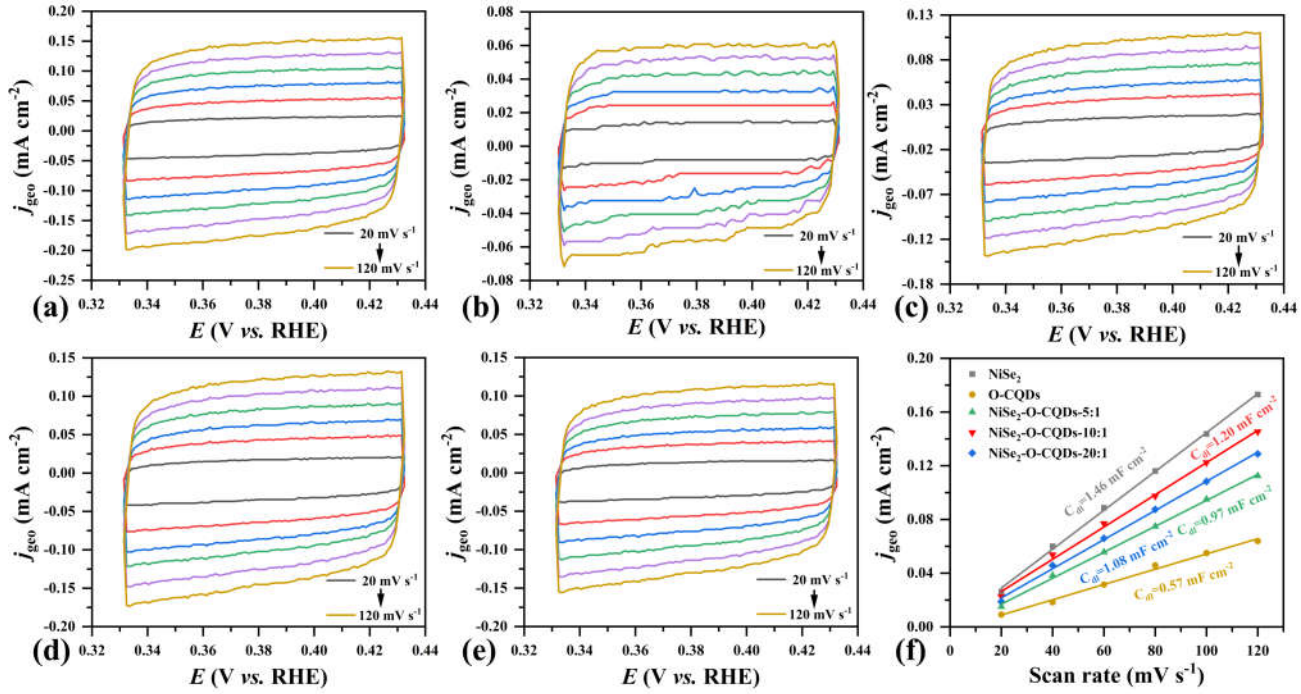

Fig. S9. CV curves of (a) $NiSe_2$, (b) O-CQDs, (c) $NiSe_2$-O-CQDs-5:1, (d) $NiSe_2$-O-CQDs-10:1, and (e) $NiSe_2$-O-CQDs-20:1 in 0.1 M KOH solution at different scan rates. (f) Double-layer capacitance (C_{dl}) plots of $NiSe_2$, O-CQDs and $NiSe_2$-O-CQDs-*X*:1 (*X* = 5, 10, 20).

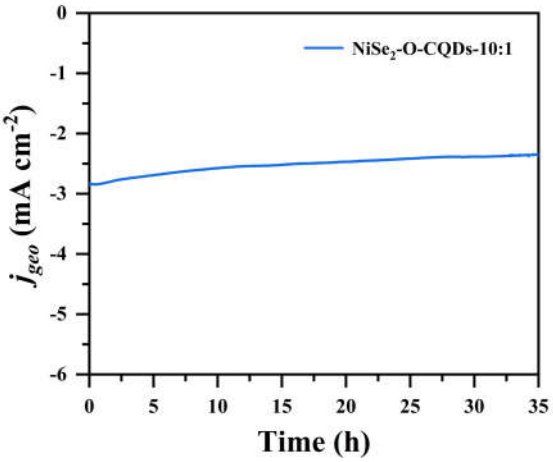

Fig. S10. Chronoamperometric curve of $NiSe_2$-O-CQDs-10:1 at 0.40 V *vs.* RHE.

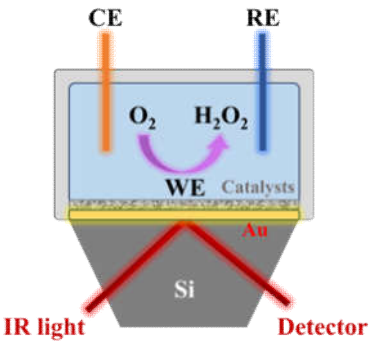

Fig. S11. Schematic diagram of the experimental setup for in-situ ATR-IR measurements

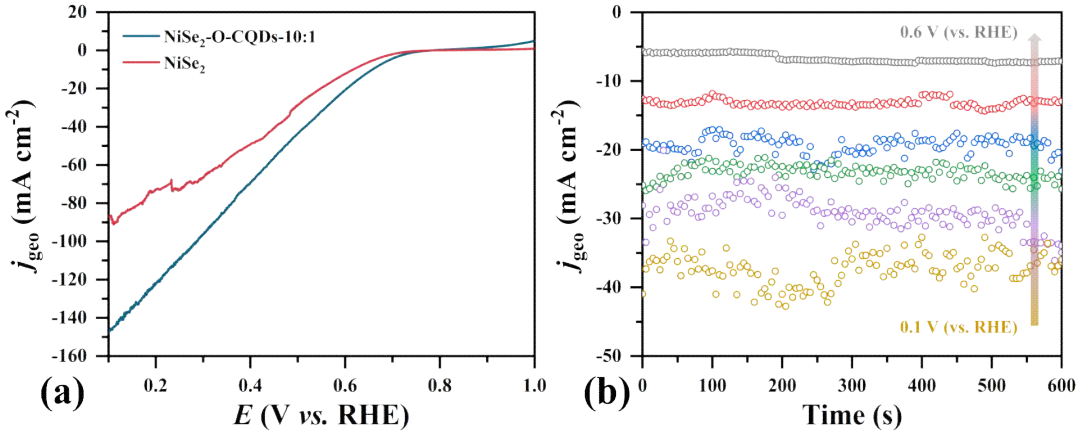

Fig. S12. Evaluation of H_2O_2 electrosynthesis performance was conducted in a continuous flow cell. (a) LSV curves of the $NiSe_2$ and $NiSe_2$-O-CQDs-10:1. (b) The *i-t* plots of $NiSe_2$-O-CQDs-10:1 at different voltages (0.1-0.6 V *vs*. RHE).

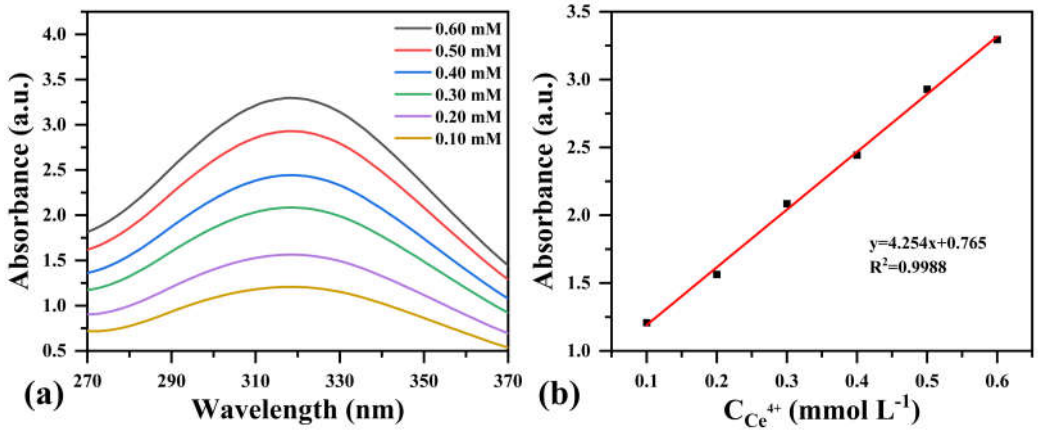

Fig. S13. (a) UV-Vis spectra of different concentrations of ceric sulfate solution (λ = 319 nm). (b) The obtained calibration curve of UV-Vis absorbance vs. $Ce(SO_4)_2$ concentration.

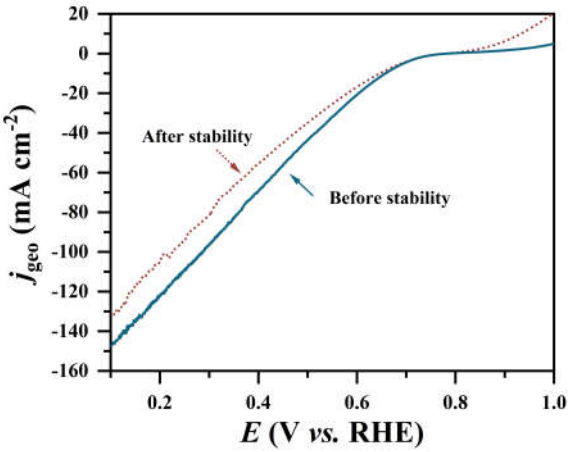

Fig. S14. LSV curves of the $NiSe_2$-O-CQDs-10:1 before and after stability tests.

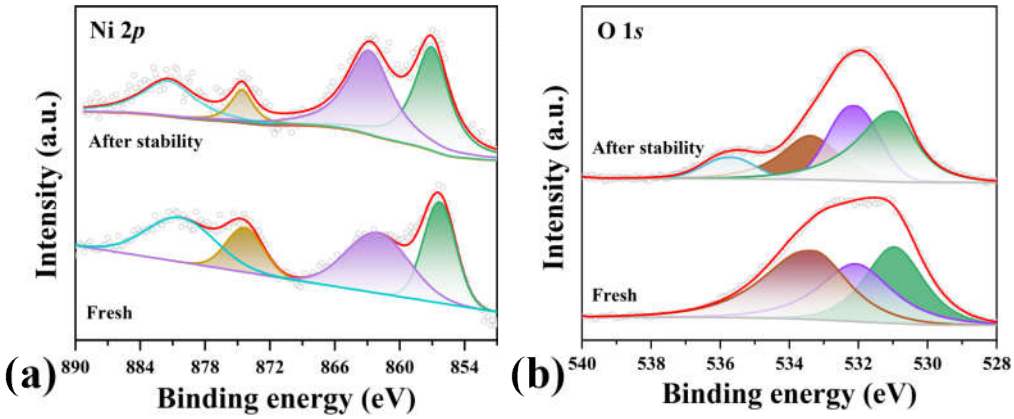

Fig. S15. XPS spectra of (a) Ni 2*p* and (b) O 1*s* for the $NiSe_2$-O-CQDs-10:1 before and after stability tests.

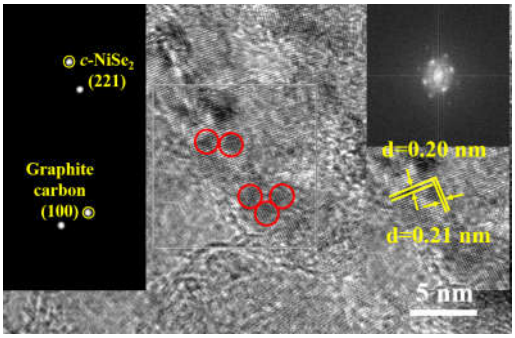

Fig. S16. HRTEM image of $NiSe_2$-O-CQDs-10:1 after the stability test.

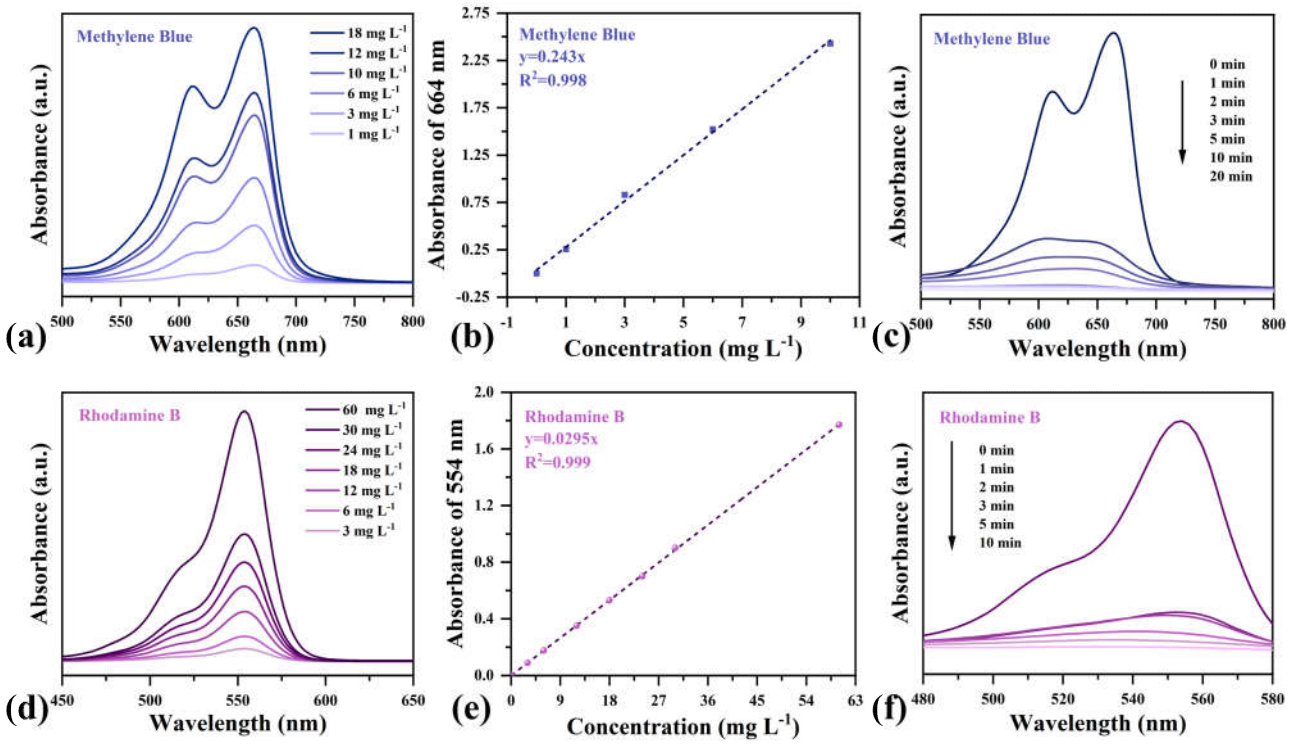

Fig. S17. UV-Vis spectra and calibration fitting curves during the decomposition process of Methylene blue (a–c) and Rhodamine B (d–f).

Table S1. Structural properties obtained from Rietveld Refinement for $NiSe_2$ and $NiSe_2$-O-CQDs samples.

Sample	Phase	Space group	a, b, c / Å	< d > / nm
$NiSe_2$	$NiSe_2$	$Pa\ \bar{3}$	5.9589 (1.3E−4)	208.6 (2.9)
$NiSe_2$-O-CQDs-10:1	$NiSe_2$	$Pa\ \bar{3}$	5.9569 (2.1E−4)	184.0 (3.6)

Table S2. EXAFS data fitting results.

Sample	Path	*CN*[a]	*R* (Å)[b]	σ^2 (Å^2)[c]	ΔE_0 (eV)[d]	*R* factor
			Ni *K*-edge (S_0^2 = 0.71)			
Ni foil	Ni–Ni	12.0*	2.47 ± 0.003	0.0054	5.56 ± 0.62	0.0029
Ni–$NiSe_2$	Ni–Se	6.02 ± 0.66	2.45 ± 0.007	0.0090	-9.0	0.0106
	Ni–Ni	2.62 ± 0.48	2.54 ± 0.018		9.0	
Ni–$NiSe_2$-O-CQDs-10:1	Ni–O	1.59 ± 0.39	2.17 ± 0.02	0.004	10.0	0.0139
	Ni–Se	2.18 ± 0.40	2.55 ± 0.01	0.004		
	Ni–Ni	1.57 ± 0.43	2.43 ± 0.01	0.003	-9.0	
			Se *K*-edge (S_0^2 = 1.01)			
Se foil	Se–Se	2.0*	2.38 ± 0.004	0.004	6.64 ± 1.15	0.0057
Se–$NiSe_2$	Se–Se	1.16 ± 0.24	2.40 ± 0.01	0.003	8.0	0.0106
	Se–Ni	3.83 ± 0.52	2.49 ± 0.01	0.010	9.0	
Se–$NiSe_2$-O-CQDs-10:1	Se–O	0.59 ± 0.14	1.66 ± 0.02	0.008	2.0	0.0160
	Se–Se	1.40 ± 0.25	2.41 ± 0.009	0.005	-9.0	
	Se–Ni	2.97 ± 0.20	2.41 ± 0.01	0.009	6.0	

[a]*CN*, coordination number; [b]*R*, the distance between absorber and backscatter atoms; [c]σ^2, the Debye Waller factor value; [d]ΔE_0, inner potential correction to account for the difference in the inner potential between the sample and the reference compound; R factor indicates the goodness of the fit. S_0^2 was fixed to 0.710 and 1.01, respectively,

according to the experimental EXAFS fit of Ni and Se foil by fixing *CN* as the known crystallographic value. * This value was fixed during EXAFS fitting, based on the known structure of Ni and Se. Fitting conditions: *k* range: 3.0–11.0; *R* range: 1.0–3.0; fitting space: *R* space; *k*-weight = 3. A reasonable range of EXAFS fitting parameters: $0.700 < S_0^2 < 1.000$; $CN > 0$; $\sigma^2 > 0$ Å^2; $|\Delta E_0| < 10$ eV; *R* factor < 0.02.

Table S3. Comparison of $2e^-$ ORR catalytic performance.

Catalysts	Synthesis steps	E_{onset} (V)	H_2O_2%	Stability/ Cell type	Yield (mmol g_{cat}^{-1} h^{-1})	Refs.
$NiSe_2$-O-CQDs-10:1	Coprecipitation, selenization at 400°C and Hydrothermal method	0.68	97.33	100 h/Flow cell	7379.51	This work
PACN-F-KOH	One-step free-radical polymerization of acrylonitrile, stabilization and pyrolysis	0.77	90	40 h/RRDE	816	[5]
Bi/PNC-4	Pyrolysis at 800°C (180 min)	-	97.75	90 h/Flow cell	2760	[6]
COF-366-Co	Impregnation method and a solvothermal reaction for imine condensation	-	91%	3 h/H-type cell	909	[7]
CoPc@OCW	Pre-carbonization, KOH activation, 900°C carbonization, acid oxidation and impregnation		99	24 h/Flow cell	10400	[8]
Co-N-C	Low-energy ball milling and flash-pyrolysis in Ar atmosphere	0.95	80	6 h/Flow cell	4330	[9]
CB-Plasma	Treating with plasma under 20% O_2/Ar atmosphere	0.80		8.3 h/H-type cell	115.92	[10]
N-DCDs	Hydrothermal method, purification by centrifugation and dialysis	0.72	99	6 h/H-type cell	1302.14	[11]
Al-MOF NSs-1	Self-template solvothermal method	0.68	98	11 h/RRDE	2560	[12]
N-FLG-8	A two-step polymerization	0.80	95	50 h/H-type cell	9660	[13]

	and carbonization under Ar atmosphere					
Ni-N_2O_2/C	Impregnation method and pyrolysis at 300°C	-	90	8 h/Flow cell	5900	[14]
Ni-N-C	Pyrolysis at 900°C	0.82	97	100 h/Flow cell	930	[15]
Sb-NSCF	Impregnation method and pyrolysis	0.76	97.2	75 h/Flow cell	7460	[16]
SC-1	Ball milling and pyrolysis at 1000°C	0.74	93.6	12 h/Flow cell	2910	[17]
O-CDs	Solvothermal method	0.703	96.55	10 h/Flow cell	3268.07	[18]
Zn_2SnO_4/SnO_2	Solvothermal method and pyrolysis at 800°C	0.67	96.75-98	24 h/RRDE	8190	[19]
Ni-SAC	Hydrothermal method, pyrolysis and acid etching	0.857	73	35 h/Flow cell	7300	[20]
o-CQD-3	Hydrothermal method and purification by dialysis	-	96.2	120 h/Flow cell	338.7	[21]
S_{10}RGO	Pre-purification and pyrolysis at 160°C and 500°C	0.773	95	40 h/Flow cell	1853.85	[22]
c-MOF Ni-250	Stirring at room temperature and pyrolysis at 300°C	0.75	95	2000 cycles/RRDE	510	[23]

References

[1] G. Kresse, Joubert, D., *Phys. Rev. B*, **1999**, 59, 1758.

[2] J.P. Perdew, K. Burke, M. Ernzerhof, *Phys. Rev. Lett.*, **1996**, 77, 3865-3868.

[3] S. Grimme, J. Antony, S. Ehrlich, H. Krieg, *J. Chem. Phys.*, **2010**, 132, 154104.

[4] R. Dronskowski, P.E. Bloechl, *J. Phys. Chem.*, **1993**, 97, 8617-8624.

[5] H. Gong, L. Wei, S. Chen, Z. Chen, T.F. Jaramillo, Z. Bao, *Nano Res.*, **2023**, 16, 11556-11563.

[6] Z. Bao, J. Zhao, S. Zhang, X. Peng, Y. Shao, C. Jiang, Z. Xu, X. Zhong, Z. Yao, J. Wang, *Nano Res.*, **2023**, 16, 9050-9058.

[7] C. Liu, H. Li, F. Liu, J. Chen, Z. Yu, Z. Yuan, C. Wang, H. Zheng, G. Henkelman, L. Wei, Y. Chen, *J. Am. Chem. Soc.*, **2020**, 142, 21861-21871.

[8] Y. Liu, S. Liu, J. Jiang, X. Wei, K. Zhao, R. Shen, X. Wang, M. Wei, Y. Wang, H. Pang, B. Li, *Adv. Mater.*, **2025**, 37, 2502197.

[9] Y. Sun, L. Silvioli, N.R. Sahraie, W. Ju, J. Li, A. Zitolo, S. Li, A. Bagger, L. Arnarson, X. Wang, T. Moeller, D. Bernsmeier, J. Rossmeisl, F. Jaouen, P. Strasser, *J. Am. Chem. Soc.*, **2019**, 141, 12372-12381.

[10] Z. Wang, Q. Li, C. Zhang, Z. Cheng, W. Chen, E.A. McHugh, R.A. Carter, B.I. Yakobson, J.M. Tour, *ACS Catal.*, **2021**, 11, 2454-2459.

[11] J. Shen, X. Qiu, Y. Zhu, *J. Mater. Chem. A*, **2023**, 11, 11704-11711.

[12] Z. Zhang, J. Guo, Z. Fang, Y. Zheng, L. Zhang, X. Liang, R. Liu, J. Zhao, W. He, L. Lu, W. Chen, *Electrochim. Acta*, **2024**, 482, 143989.

[13] L. Li, C. Tang, Y. Zheng, B. Xia, X. Zhou, H. Xu, S.Z. Qiao, *Adv. Energy Mater.*, **2020**, 10, 2000789.

[14] Y. Wang, R. Shi, L. Shang, G.I.N. Waterhouse, J. Zhao, Q. Zhang, L. Gu, T. Zhang, *Angew. Chem. Int. Ed.*, **2020**, 59, 13057-13062.

[15] H. Shen, L. Pan, T. Thomas, J. Wang, X. Guo, Y. Zhu, K. Luo, S. Du, H. Guo, G.J. Hutchings, J.P. Attfield, M. Yang, *Cell Rep. Phys. Sci.*, **2020**, 1, 100255.

[16] M. Yan, Z. Wei, Z. Gong, B. Johannessen, G. Ye, G. He, J. Liu, S. Zhao, C. Cui, H. Fei, *Nat. Commun.*, **2023**, 14, 368.

[17] Y. Wu, Z. Shen, Q. Yuan, Y. Zhao, X. Xu, K. Sun, A. Wang, H. Sun, B. Li, S. Hu, R. Xu, Z. Wang, J. Jiang, M. Fan, *ACS Sustain. Chem. Eng.*, **2025**, 13, 5178-5189.

[18] X. Shen, Z. Wang, H. Guo, Z. Lei, Z. Liu, L. Wang, *Small*, **2023**, 19, 2303156.

[19] Y. Yang, A. Xu, Y. Ren, K. Li, K. Nie, Y. Huang, H. He, J. Xu, X. Yin, *Appl. Catal. B: Environ.*, **2025**, 361, 124625.

[20] Y. Sun, K. Fan, J. Li, L. Wang, Y. Yang, Z. Li, M. Shao, X. Duan, *Nat. Commun.*, **2024**, 15, 6098.

[21] L. Xie, C. Liang, Y. Wu, K. Wang, W. Hou, H. Guo, Z. Wang, Y.M. Lam, Z. Liu, L. Wang, *Small*, **2024**, 20, 2401253.

[22] S. Li, S. Du, J. Li, W. Fan, Y. Yang, P. Zhao, H. Zhu, W. You, X. Sang, F. Zhang, *Chem. Sci.*, **2025**, 12178-12188.

[23] H. Wu, T. He, M. Dan, L. Du, N. Li, Z. Liu, *Chem. Eng. J.*, **2022**, 435, 134863.